Jacob's ladder of approximations to paraxial dynamic electron scattering

A. Lubk
Triebenberg Laboratory, Institute of Structure Physics, Technische Universität Dresden, 01062 Dresden, Germany

J. Rusz
Department of Physics and Astronomy, Uppsala University, Box 516, 75120 Uppsala, Sweden
(Received 29 September 2015; published 7 December 2015)

Dynamical scattering theory describes the dominant scattering process of beam electrons at targets in the transmission electron microscope (TEM). Hence, practically every quantitative TEM study has to consider its ramifications, typically by some approximate modeling. Here, we elaborate on a hierarchy within the various approximations focusing on the two principal approaches used in practice, Bloch wave and multislice. We reveal characteristic differences in the capability of these methods to reproduce the correct local propagation of the wave function, while convergent results are obtained over larger propagation distances. We investigate the dependency of local variations of the wave function on the atomic number of the atomic scatterers and discuss their significance for, e.g., inelastic scattering.

DOI: 10.1103/PhysRevB.92.235114 PACS number(s): 61.05.J−, 34.80.Bm, 79.20.Uv, 68.37.−d

I. INTRODUCTION

The remarkable success of transmission electron microscopy (TEM) as a characterization tool in the materials sciences rests mainly on two pillars. First, elaborate electron sources and optics allow the production, imaging, and detection of electron beams with ever increasing signal and spatial resolution. Second, the strong Coulomb interaction between the beam and the highly localized electric potentials of the atoms results in large intensities even at large scattering angles. The combination of these two aspects allows the retrieval of the structure of atomic assemblies, including its internal symmetries and composition, with sub-angstrom spatial resolution.

However, the strong Coulomb interaction proved to be both boon and bane, as the validity of the first-order Born approximation is severely limited within the scope of TEM investigations. The derivation of a target's structure including possible symmetries from scattering cross sections is therefore not as straight forward as, e.g., in x-ray diffraction. This obstacle has been appreciated since the heyday of electron diffraction, prompting the development of the dynamical scattering theory as opposed to the first-order Born approximation (i.e., kinematic scattering). Important contributions have been given by Bethe [1], Lamla [2], Cowley and Moodie [3], Fujimoto [4], Howie and Wheelan [5], Fujiwara [6], Kambe [7], Berry [8], and Gratias and Porter [9], to name just a few (see, e.g., [10] for a more comprehensive account). By now, it is well understood that the interpretation of atomic resolution images acquired with a TEM has to be done using dynamic theory. That also pertains to three-dimensional atomic structure determination [11], spin and orbital momentum mapping based on electron microscopic magnetic dichroism [12], nanoscale elemental mapping [13,14], or high-angle annular dark field scanning TEM structure mapping [15], to give just a few examples.

Usually, there is no analytical solution to the dynamic scattering equation. Moreover, several limitations prevent a computationally feasible numerical solution of the complete problem, including, e.g., effects such as backscattering from the target. Accurate approximations are therefore required and large and ongoing efforts have been put into the development of such (e.g., [16–19]). Important parameters in these computations are numerical efficiency and simplicity of implementation, which need to be balanced against accuracy. A quantitative understanding of the errors involved in the approximations is therefore indispensable.

The starting point of the dynamic scattering formalism is an approximation of the Klein-Gordon equation valid for small-angle scattering referred to as the paraxial scattering approximation (e.g., [20]; the nonparaxial regime is considered in, e.g., Refs. [21,22]). This equation is mathematically equivalent to a two-dimensional time-dependent Schrödinger equation with the optical axis z taking the place of the time coordinate [8] and both energy and momentum being relativistically corrected. Consequently, similar solutions and approximation strategies may be applied. The main difficulty is presented by the peaked z dependency introduced by the atomic scatterers, which would correspond to pulse-train-like potentials in the time-dependent analog. The various approximations put forward can be classified into two main lines.

One class of algorithms utilizes numerical integrators of the paraxial equation, which are either borrowed from numerical integration (NI) [22,23] or semianalytically computed for fixed step sizes [3]. The latter approach, referred to as multislice (MS), is typically used with a step size comprising one sheet of atoms, which permits a particularly fast numerical execution. Both integration schemes converge to the exact solution of the paraxial equation in the limit of small integration step sizes [24,25].

The other class of algorithms seeks the solution in two steps: first a basis of solutions is generated by diagonalizing the paraxial Hamiltonian, and second, the initial wave is expanded into this basis. To compute the basis function one typically employs periodic boundary conditions. Hence, the basis functions are Bloch waves and the algorithms are termed Bloch wave methods. Depending on whether one includes the z direction (optical axis, propagation direction) in the expansion, one speaks of 2D or 3D Bloch wave methods (2D/3D-BW). Because of the numerical scaling of the eigenvalue problem

Bloch wave methods are typically less favorable if the basis is very large, i.e., if a large number of scattering directions has to be considered. A large class of scattering problems, however, allows for a sufficient reduction of the basis, rendering Bloch wave methods a valuable alternative to direct integration schemes such as MS. In particular the basis truncation along the z direction, corresponding to 2D-BWs, leads to a simple analytic z dependency that can be favorably exploited under various circumstances. For instance, the prominent two-beam case [5], where only one particular scattered beam additional to the unscattered one is dominating, can be solved analytically. Similarly, the calculation of inelastic scattering matrix elements for electron energy loss spectra can be efficiently organized by exploiting analytic expansions of the Bloch waves. Moreover, a diagrammatic technique [9] as applied in time-dependent perturbation theory [26] uses the analytic 2D-BW solution as zero-order approximation in a perturbative treatment of the z dependency. Additionally, the separability of z and the lateral x,y dimensions in the 2D-BW method allow further approximations borrowed from band computation methods in solid state physics, notably the channeling approximation [27].

The MS and the BW methods are the cornerstones of various dynamic scattering simulation codes (e.g., [16,17,20,28,29]) used for simulating high-resolution images, diffraction patterns, electron energy loss spectra, and other signals recorded in the TEM. The above introduction has shown that the accuracy of the direct integration schemes and the Bloch wave approaches are closely related to the integration step size and the size of the Bloch wave basis, respectively. In the following we will elaborate on a classification based on the z dependency of the various approximations. To that end we revisit the analytical derivation of the above methods and perform a numerical study.

II. SCATTERING THEORY

We start off with what could be considered as the basic equation for elastic electron scattering in the TEM operated in the medium and high acceleration voltage regime, the stationary Klein-Gordon equation in the high-energy (omitting V^2) and paraxial (separating a fast and slowly oscillating wave along the optical axis z and omitting second-order derivatives of the latter) approximation

$$i\,\partial_z \Psi(\mathbf{r},z) = \underbrace{\left(-\frac{1}{2k}\Delta - \frac{1}{v}\Phi\right)}_{\hat{H}=\hat{T}+\hat{U}}\Psi(\mathbf{r},z). \tag{1}$$

Here, k denotes the wave number of the fast electron wave, v its velocity, and Φ the electrostatic potential. We furthermore employ atomic units ($e = m_e = \hbar = 1$) and we distinguish between the kinetic term $\hat{T}$ and potential term $\hat{U}$ in the paraxial Hamiltonian $\hat{H}$. A short inspection of (1) directly reveals its similarity to the time-dependent Schrödinger equation [8]. The full solution to the paraxial equation (1) can be symbolically integrated according to (see, e.g., [26]) [47]

$$|\Psi(z)\rangle = \underbrace{\hat{\mathcal{Z}}\exp\left(-i\int_0^z \hat{H}(z')dz'\right)}_{\hat{K}(z;0)}|\Psi(0)\rangle, \tag{2}$$

where $\hat{\mathcal{Z}}$ denotes the z-ordering operator in analogy to Dyson's time-ordering operator and $\hat{K}(z;z')$ is the z-evolution operator corresponding to the time-evolution operator (the propagator). The z ordering is frequently disregarded in the pertinent literature [20,30,31], which can lead to considerable misconceptions when considering certain approximations later on.

One may now employ a multitude of numerical methods to integrate the above equation. A straight choice consists of choosing a numerical integrator, i.e., a step-by-step propagation along z, which is well adapted to the problem [22,23]. The error pertaining to the numerical integration accumulates with propagation distance (crystal thickness t) and can be reduced by decreasing the integration steps. Current implementations of these methods still require considerable computation time, which can be overcome by fixing the step size and approximating the propagator by analytical expressions. This leads to the popular MS method [3], which consists of an alternate application of the free-space propagator

$$\hat{K}_T(\delta z) := \exp(-i\underbrace{(z-z')}_{\delta z}\hat{T}) \tag{3}$$

and the transmission operator

$$\hat{K}_U(z;z') := \exp\left(\int_{z'}^{z} U(z'')dz''\right) \tag{4}$$

according to

$$|\Psi(z_N)\rangle = \prod_{n=0}^{N-1}\hat{K}_T(\delta z_n)\hat{K}_U(z_{n+1};z_n)|\Psi(z_0)\rangle. \tag{5}$$

The transmission operator diagonalizes in position space where it is referred to as transmission function, and the free-space propagator, referred to as Fresnel propagator, diagonalizes in Fourier space. Accordingly, the successive application of transmission operator and free-space propagator can be performed very efficiently by switching between position and Fourier space.

In the limit $\delta z \to 0$ the MS algorithm converges to the true solution [24]; however, in order to reduce computation time, one integration step δz is typically chosen so as to comprise an equivalent of one atomic layer (i.e., $\delta z \approx 1$ Å) in a crystal (referred to as atomic MS in the following). The accuracy of this choice stems from the quasidiscrete nature of the atomic scattering potentials within a large, almost potential-free atomic interspace, the atomic lattice. This particular potential structure allows for transmitting the wave with only the transmission operator (i.e., neglecting free-space propagation) through thin sheets containing atoms and propagating the wave without influence of the potential in the atomic interspace (see Fig. 1). Consequently, the atomic MS algorithm basically consists of a particular, well-adapted approximation of the paraxial equation (1) omitting either the kinetic or potential term within certain z intervals. This renders the evaluation of the z ordering trivial because we do not have to consider the nonvanishing commutator between the kinetic and potential operator. Similarly to other numerical integration schemes, the difference between the (atomic) MS solution and the exact solution grows with the propagation distance.

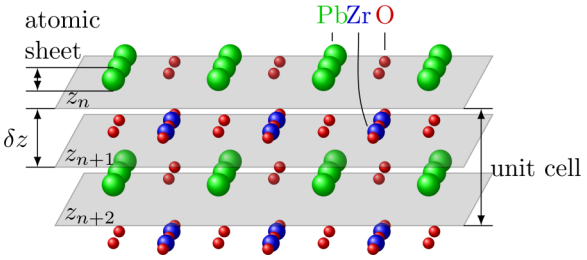

FIG. 1. (Color online) Working principle of the MS approximation. The strongly localized atomic potentials exert a dominant influence in thin sheets only, where the concomitant propagation may be neglected therefore. In turn, the potential influence is negligible in the atomic interspace. The depicted crystal structure pertains to $PbZrO_3$ oriented in the [001] direction and the periodicity in the z direction is indicated.

The 2D-BW formalism may now be derived from the MS method in the following way. We first note the Zassenhaus expansion (following from the Baker-Campbell-Haussdorf formula [32]) truncated after the third factor

$$e^{t(\hat{A}+\hat{B})} = e^{t\hat{A}}e^{t\hat{B}}e^{-\frac{t^2}{2}[\hat{A},\hat{B}]}\ldots \tag{6}$$

with some arbitrary operators $\hat{A}$ and $\hat{B}$. Consequently, if the norm of the commutator

$$\left\| \frac{t^2}{2}[\hat{A},\hat{B}] \right\| \ll 1 \tag{7}$$

is small, we may approximate the product of the exponentials by the exponential of the sum of the two operators

$$e^{t\hat{A}}e^{t\hat{B}} \approx e^{t(\hat{A}+\hat{B})}. \tag{8}$$

If we now substitute $\hat{A} = \hat{K}_U$, $\hat{B} = \hat{K}_T$, and $t = z_{n+1} - z_n = a_z$, where the slice thickness was chosen such to comprise one unit cell with lattice parameter a_z, we obtain

$$\Psi(\mathbf{r},z_{n+1}) = \exp\left[i\left(\frac{1}{2k}\Delta + \frac{1}{v}\overline{\Phi}(\mathbf{r}) \right) a_z \right] \Psi(\mathbf{r},z_n), \tag{9}$$

where the projected potential

$$\overline{\Phi}(\mathbf{r}) = \int_{z_n}^{z_{n+1}} \Phi(\mathbf{r},z)dz/a_z \tag{10}$$

has been introduced. Because we have chosen a slice thickness of one unit cell, the exponential in (9) does not depend on z anymore (note the absence of the z ordering) and (9) is the formal solution to the constituting equation of the 2D-BW formalism [1,5,7]

$$i\,\partial_z \Psi(\mathbf{r},z) = \left[-\frac{1}{2k}\Delta - \frac{1}{v}\overline{\Phi}(\mathbf{r}) \right] \Psi(\mathbf{r},z), \tag{11}$$

where the z dependency of the paraxial Hamiltonian has vanished. Accordingly, the propagation diagonalizes in the eigenspace of the Hamiltonian. 2D-BW methods exploit that property by diagonalizing the above Hamiltonian and expanding the 2D incoming wave at the entrance face of the crystal into the corresponding basis (2D-BWs). The wave at any z coordinate is then readily obtained by the analytic z dependency of the 2D-BWs without additional effort.

The above derivation contained two approximations, which lead to the following characteristic deviations of the 2D-BW method compared to exact solutions. First, the slice thickness was set to one unit cell, which may be significantly smaller in the direct integration schemes. As a consequence, the internal structure and symmetries of the unit cell determining the strength of systematic scattering directions into higher-order Laue zones is absent from 2D-BW calculations. Second, the commutator between transmission and propagation operator

$$\begin{aligned} -\frac{a_z^2}{2}[\hat{K}_U,\hat{K}_T] &= -\frac{a_z^2}{4kv}[\nabla\overline{\Phi}(\mathbf{r})\nabla + \Delta\overline{\Phi}(\mathbf{r})] \\ &= \frac{a_z^2}{4kv}[\overline{\mathbf{E}}(\mathbf{r})\nabla + \overline{\rho}(\mathbf{r})] \end{aligned} \tag{12}$$

may become large due to the diverging electric field $\mathbf{E}$ at the site of the atomic core, which, in spite of the smallness of the prefactor, leads to a certain violation of the approximation (9). Given the singular nature of this peak in position space this mainly translates into an erroneous behavior of the 2D-BW solution close to atomic sites. The large lateral spatial frequency components of that peak will quickly disperse upon propagation, dampening the discrepancy at larger distance to the atom. A vivid picture of that behavior will be given in the next section. Note that in the literature the derivation of 2D-BW method is more commonly presented in a different way. Equation (11) is obtained directly by replacing the three-dimensional z-dependent potential $\Phi(\mathbf{r})$ in Eq. (1) by its two-dimensional z-projected version $\bar{\Phi}(x,y)$. However, as will be shown below, the atomic multislice is a very good approximation and the derivation of the 2D-BW from atomic multislice provides instructive insight about the neglected commutator, which is implicitly also present, when the z-projected potential is introduced.

Within the framework of Floquet theory [33], the approximations leading to the 2D-BW method may be dropped as detailed in Appendix A, which allows taking into account *periodic* variations of the potential along z exactly. In practice one commonly deviates from the Floquet solution by invoking an expansion into a 3D Bloch wave basis, which is obtained from diagonalizing the original nonparaxial Klein-Gordon equation with a z-dependent periodic potential Φ, i.e.,

$$\Psi(\mathbf{r}) = \sum_n C^{(n)} e^{iq_z^{(n)}z} \sum_{\mathbf{g}} u_{\mathbf{g}}^{(n)} e^{i\mathbf{g}\mathbf{r}}. \tag{13}$$

Here $\mathbf{g}$ denotes reciprocal lattice vectors, the $u_{\mathbf{g}}^{(n)}$ are the Fourier coefficients, and $q_z^{(n)}$ the Bloch vector of the nth Bloch wave. We furthermore assumed a plane incident wave along z (no lateral components in the Bloch vector). The expansion coefficients $C^{(n)}$ are typically *approximated* by projecting the *unperturbed* incoming (instead of the true scattered) wave $\Psi^{(0)}$ on the periodic part of the Bloch wave basis within the first unit cell in 3D according to [34]

$$C^{(n)} \approx \int_\Omega u^{(n)*}(\mathbf{r})\Psi^{(0)}(\mathbf{r})d^3r. \tag{14}$$

Consequently, two approximations with respect to the Floquet solution are involved in the 3D-BW approach, first the use of the unperturbed instead of the true wave and second the projection on the periodic instead of the full Bloch wave

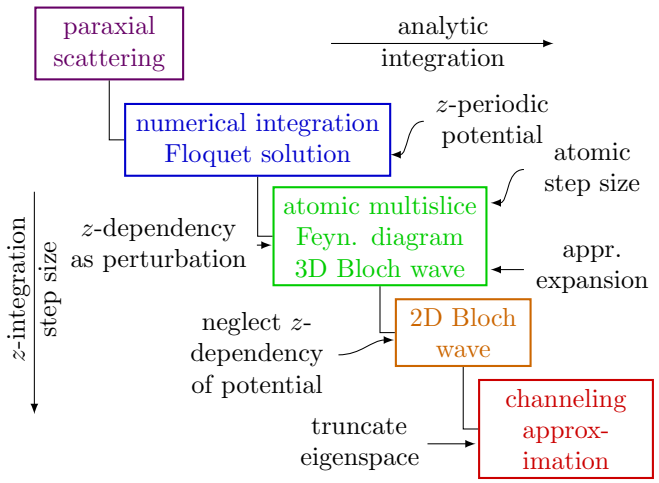

FIG. 2. (Color online) Hierarchy of numerical approximations for the dynamic scattering problem. The order roughly scales with the characteristic integration step size leading to a higher level of analytic description of the propagation along z.

basis. These approximations seem to have been previously overlooked in the pertinent literature (e.g., [34]). The error of this 3D-BW approximation grows with increasing atomic weight increasing the neglected modulations of the wave in the first unit cell. This error does not accumulate as the propagation distance grows. A second error stems from the deviations of the computed 3D-BW basis including the Bloch vectors from the exact ones, which leads to an increasing mismatch of the 3D-BW solution with growing propagation distance.

Summing up the above analytical considerations, we end up with a Jacob's ladder of approximations applied to the dynamic scattering problem depicted in Fig. 2. An "exact" solution is obtained by integrating the paraxial scattering equation with some numerical or semianalytical integration algorithm such as Runge-Kutta or MS with sufficiently small step size. In the case of z-periodic potentials, the same level of approximation is obtained by the Floquet solution, invoking direct integration schemes for the first unit cell. In practice, the accurate reproduction of the z dependency is sacrificed to obtain acceptable computation times and/or analytical simplicity. The most radical approximation, i.e., the 2D Bloch wave method, completely neglects the z-dependent potential structure, which allows for a full analytic description of the z propagation within the eigenspace of the 2D-BW Hamiltonian. The region in between the exact solutions and that of 2D-BWs is filled by atomic MS integrating over atomic sheets, diagrammatic perturbation schemes, and the 3D-BW method.

III. NUMERICAL STUDIES

To supplement and detail the above analytical arguments we have performed numerical scattering simulations based on numerically integrating Eq. (1) with very small step sizes (the NI solution), solving Eq. (5) with atomic step size (the MS solution), and computing the 3D- and 2D-BW solutions. In order to allow for a maximal comparability (in terms of sampling, algorithms, etc.), we use the same numerical integration algorithm (Adams-Bashforth-Moulton PECE [35] as implemented in the ode113 routine of Matlab) for the NI and the 2D-BW solution instead of performing the (expensive) diagonalization of the BW Hamiltonian with a large number of beams ($96 \times 96 = 9216$ in our case). We applied the Laplace operator in Fourier space in order to avoid any discretization error involved when using a real space approximation [23]. The 3D-BW solution is obtained on a truncated basis consisting of $\mathbf{g}$ vectors, for which the dimensionless product $w_{\mathbf{g}}$ of excitation error $s_{\mathbf{g}}$ with extinction distance $\xi_{\mathbf{g}}$ fulfills $w_{\mathbf{g}} < 10^4$. This results in a basis size is 3649. Into the final summation we only included terms for which the product of Bloch coefficients was above 5×10^{-7}. The procedure follows the first steps of the MATS algorithm introduced in Ref. [36] for inelastic scattering calculations.

As test target we used the high-temperature cubic perovskite phase of $PbZrO_3$ (space group $Pm3m$, $a = 4.18$ Å, orientation [1,0,0]; see Fig. 1), because it represents a relatively simple test structure combining light and heavy elements thereby covering different scattering regimes. The maximal thickness was set to $t = 24\,a \approx 10$ nm in order to cover the typical thickness range used in high-resolution TEM studies [37]. The crystal potential was assembled from neutral independent atoms parametrized according to Ref. [38] (see Refs. [20,39] for alternative ones). Further simulation parameters are 200 kV acceleration voltage and a spatial sampling of 4.4 pm. Note that the ramifications of the thermal motion of the lattice have been completely ignored. They may be taken into account by performing an expensive frozen lattice summation of the results corresponding to the imaging conditions [40], which represents a further level of complexity and is beyond the scope of this study. For the same reasons aberrations of the microscope as well as the ramifications of partial coherence have been completely ignored.

The main results of the scattering simulations are depicted in Fig. 3. The full propagation from $z = 0$ nm to $z = t$ depicted in the left column for different x-z cross sections exhibits the typical channeling effect of the electron beam along atomic columns, with the periodicity depending on the atomic weight of the column. This effect is present in all four solutions. Both the x-z cross sections as well as the x-y takeouts furthermore reveal a substantially larger amount of high-spatial frequency data in the NI, MS, and 3D-BW data compared to the 2D-BW solution. This originates mainly from the missing higher order Laue zones in the 2D-BW solution (see also Fig. 5).

We now zoom into the propagation along z to reveal the second characteristic feature of the 2D-BW approximation (right column in Fig. 3). In the NI, MS, and 3D-BW solutions we observe a characteristic beating stemming from the pulse train of atomic potentials in the z direction. It consists of a sharp ramp in the phase (due to the projected potential of the atom) followed by a rapid interference effect in the amplitude. This effect is completely absent in the 2D-BW calculation. Note, however, that after each beat the NI, MS, and 3D-BW solutions converge to the 2D-BW solution as the localized effect behind the atoms quickly disperses. One could vividly rephrase this behavior as the difference between a staccato and legato interpretation of the same melody. The deviations of the 2D-BW solution agree well with the theoretic predictions of Sec. II, where we identified a nonvanishing strongly peaked

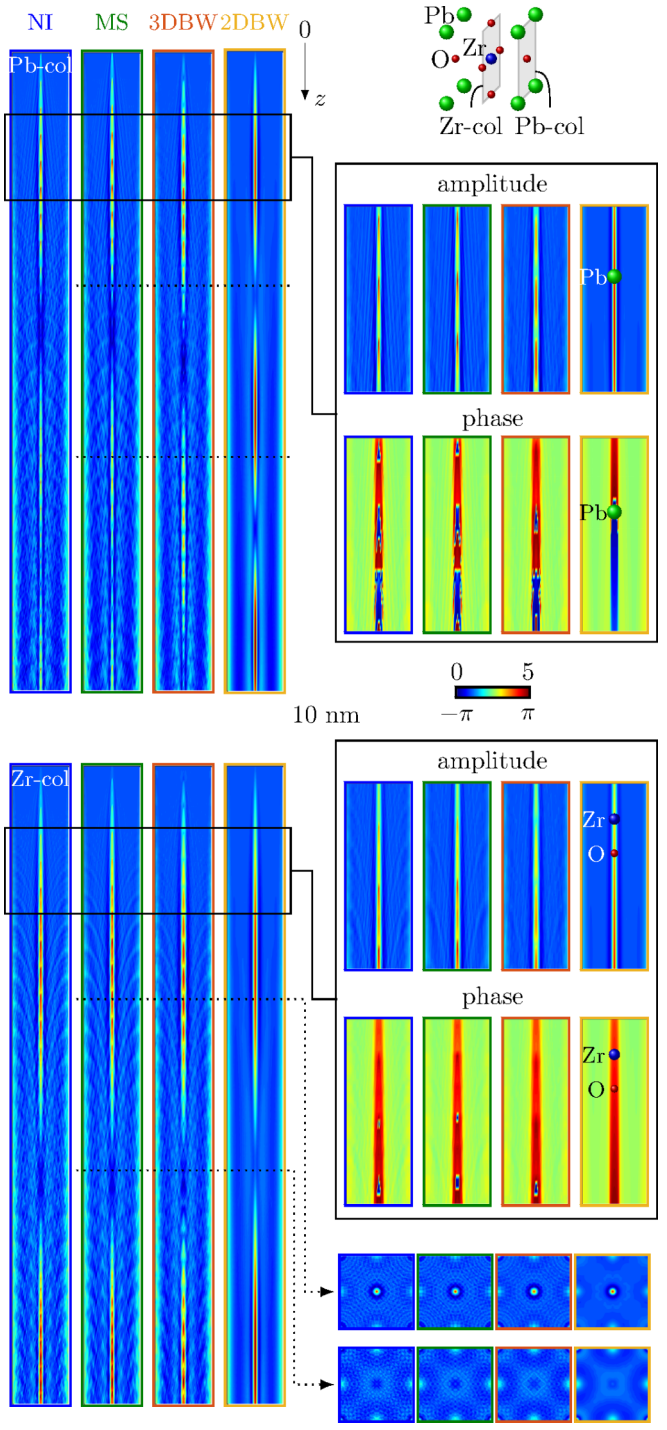

FIG. 3. (Color online) Results of the scattering simulations using the numerical integration (NI), the atomic multislice (MS), and the 3D-BW and 2D-BW formalism at various thicknesses. The visually prominent differences are mainly due to the absence of the higher order Laue zones in the 2D-BW calculations. The zoom-ins in the right column additionally reveal a beating structure of the NI, MS, and 3D-BW solution imprinted by the localized atomic potentials. Depending on the atomic weight of the scatterer the local variations can reach 1 rad in the phase and 1 in the normalized amplitude (see Pb column).

commutator as the main source of difference between the MS and 2D-BW approximation. Accordingly, the deviations are

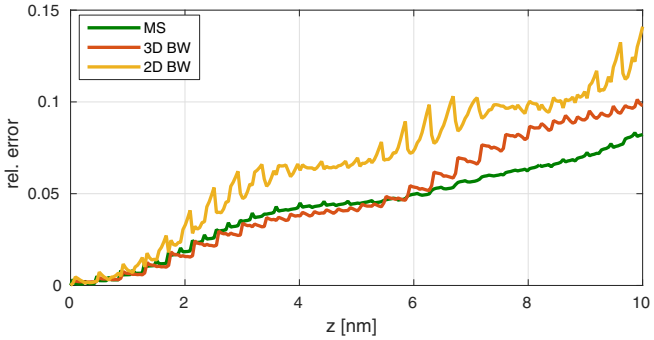

FIG. 4. (Color online) Relative error of the atomic MS, 3D-BW, and 2D-BW relative to the NI reference solution.

predicted to be more pronounced at the strongly scattering Pb column, which is confirmed by the numerical results. Moreover, we observe a significant difference between the 3D-BW solution on the one side and the NI and MS solution on the other side when focusing on the first part of the crystal (in particular the Pb column). This deviation is the consequence of the approximate computation of the 3D-BW expansion based on an unperturbed incoming wave within the first unit cell discussed previously.

The condensation of the above discussion is to be found in the evolution of the relative error of the three lower level approximations (MS, 3D, and 2D-BW) with respect to the NI solution considered as reference,

$$\epsilon(z) = \sqrt{\frac{\sum_n |\Psi(\mathbf{r}_n,z) - \Psi_{\mathrm{NI}}(\mathbf{r}_n,z)|^2}{\sum_n |\Psi_{\mathrm{NI}}(\mathbf{r}_n,z)|^2}}, \qquad (15)$$

in dependence on the propagation distance depicted in Fig. 4. The error of the 2D-BW solution is the largest and one clearly observes the periodically peaked discrepancies at the atomic sites. These peaked deviations are less pronounced in the 3D-BW and the MS solution in that order. They originate from the abrupt modulations of the wave function at the atomic potentials, which is best approximated by the MS algorithm as the order of the z expansion of the 3D-BW solution is typically limited. The MS and 2D-BW error grows with propagation distance as both solutions feature an accumulating numerical error in the course of the numerical integration. The 3D-BW solution is comparable to MS in the achieved accuracy in the beginning before deviating more strongly at larger propagation distances. Note, however, that this behavior strongly depends on the size of the basis used in the 3D-BW calculations.

To gain further insight into the deviations between the four algorithms, we compute the 3D Fourier transform of the NI, MS, and BW solutions. The results are depicted in Fig. 5. One observes an extended maximum at the center of reciprocal space, corresponding to the zeroth-order Laue zone, with an intensity distribution similar between all approximations. Outside of the center the intensity is quickly fading in the case of the 2D-BW approximation. The other approximations show intensity at reciprocal lattice points close to the Ewald sphere [48], which in contrast to kinematic scattering at thick crystals do not have to be exactly on the Ewald sphere. The characteristic rings at multiples of reciprocal lattice vectors $1/a_z$ hallmark the higher order Laue zones. Interestingly, the

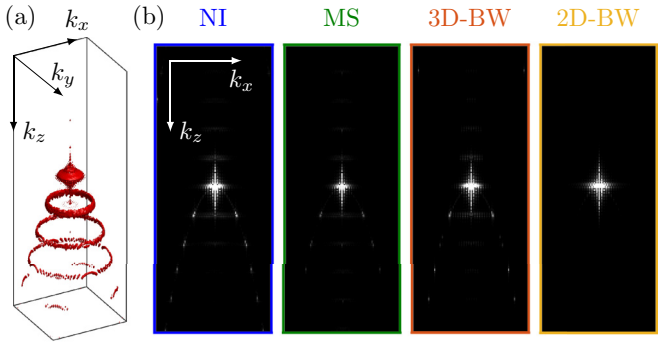

FIG. 5. (Color online) (a) 3D Isosurface from the Fourier spectrum of the NI solution illustrating the appearance of higher order Laue zones. (b) Cross sections of the 3D Fourier decomposition of the wave functions obtained from the NI, atomic MS, 3D-BW, and 2D-BW algorithms in that order.

NI, MS, and 3D-BW solution additionally contain significant intensity around $\mathbf{k} = (0,0,na_z^{-1})$ for positive and negative integers n, which confirms previous numerical studies on optimal BW basis sets for inelastic scattering simulations leading to the development of the MATS algorithm [36]. Their occurrence can be analytically explained partly by treating the scattering on z-dependent potentials within the second-order Born approximation (see Appendix B). Note furthermore that these on-axis reflections are most pronounced in the MS solution, which can be traced back to the abrupt z modulation of the wave function, when applying the transmission function in the MS algorithm.

IV. DISCUSSION

The above results raise the question of under which circumstances the observed deviations become important in practice. Two scenarios seem to be affected. The first is very accurate high-resolution studies aiming at 3D atomic structure reconstruction (e.g., [11]) or atomic charge density exploration. Owing to the higher order of approximation, direct integration schemes such as MS should be employed here. The second is investigations requiring a very accurate consideration of the z propagation around the atoms. Such a situation can occur when studying core loss or phonon losses [41,42], where the z dependency enters in the calculation of inelastic scattering matrices or mixed dynamic form factors [43]. A typical approximation employed in these computations is to approximate the z dependency of the electron wave function by the smooth analytic behavior of the 2D-BW solution [44] or to completely disregard any z modulation other than the one given by the carrier frequency (typical when using MS for the elastic scattering [13,45]). Notable exceptions are the 3D-BW computations reported, e.g., in Refs. [12,36]. In the light of the above findings these approximations leads to a small error at light elements producing a weak local modulation only. For medium and heavy elements, however, the local wave function modulation at the atomic sites comprises phase shifts up to one radian and corresponding relative amplitude variations of 100%. These modulations may significantly affect the inelastic transition probability depending on the transition considered. Numerical studies on bcc iron confirm the importance of these 3D effects for the computation of inelastic scattering [36]. Moreover, a recent comparison on electron magnetic dichroism in bcc Fe invoking a comparison between 3D-BW and MS methods corroborates the consistent error level of the latter methods up to medium light elements [46]. We note, however, that the situation may change if heavier elements are invoked, rendering the error due to the 3D-BW expansion more significant.

V. SUMMARY

We have revealed an order in the most prominent approximations to dynamic scattering, which roughly follows the integration step size involved. The most accurate approximation to the paraxial scattering equation (1) employs a numerical integrator adapting the variable step size to the required accuracy. The atomic multislice algorithm predefines the step size in the integration utilizing the sparse nature of the atomic crystal potential. It correctly reproduces the beating nature of the scattering at the atomic scatterers. The latter is also contained in 3D Bloch wave solutions, which, however, contain an error due to an approximate expansion into the 3D Bloch wave basis, which can lead to problems, when considering heavy scatterers. The 2D Bloch wave method is based on averaging the potential within one unit cell allowing for a complete analytical description of the scattered wave. It correctly reproduces the scattering averaged within one unit cell along z, but completely misses the beat. This hierarchy reveals the significance of the z dependency of the potential.

The results indicate that multislice and, with some restrictions pertaining to heavy elements, 3D Bloch wave simulations should be favored over 2D Bloch wave simulations if high accuracy is required, in particular in the vicinity of the atoms. The most important case pertains to inelastic scattering computations, where the precise shape of the electron wave functions enters in the computations of EELS or EDX spectra including resonance effects, such as white lines. A detailed study on the magnitude of this effect will be addressed in a future publication.

ACKNOWLEDGMENTS

The authors acknowledge financial support from the European Union under the Seventh Framework Programme under a contract for an Integrated Infrastructure Initiative, Reference 312483 - ESTEEM2, as well as the Swedish Research Council, Göran Gustafssons Foundation, and STINT.

APPENDIX A: FLOQUET THEORY

In this Appendix we briefly illustrate the basics of Floquet theory and its significance for paraxial electron scattering. Let $\mathbf{\Psi}(z)$ be a fundamental matrix of linearly independent solutions to the paraxial equation

$$i\partial_z \Psi(\mathbf{r},z) = \hat{H}\Psi(\mathbf{r},z) \tag{A1}$$

with a periodic potential, i.e.,

$$\hat{H}(\mathbf{r},z+a_z) = \hat{H}(\mathbf{r},z). \tag{A2}$$

According to Floquet's theorem we then have

$$\mathbf{\Psi}(z+a_z)=\mathbf{\Psi}(z)\mathbf{B} \quad \text{for} \quad \forall z, \tag{A3}$$

where the monodromy matrix

$$\mathbf{B}=\mathbf{\Psi}^{-1}(0)\mathbf{\Psi}(a_z) \tag{A4}$$

does not depend on z. The eigenvalues $\rho^{(n)}$ of $\mathbf{B}$, called the characteristic multipliers, do not depend on the particular choice of the fundamental matrix. They define the (Floquet) exponents $\mu^{(n)}$ through the relations $\rho^{(n)}=\exp(\mu^{(n)}z)$. As a consequence of Floquet's theorem we then have a solution $\Psi^{(n)}(\mathbf{r},z)=\exp(\mu^{(n)}z)u^{(n)}(\mathbf{r},z)$ with periodic $u^{(n)}(\mathbf{r},z)$. Consequently, the Floquet exponents play the role of the Bloch vector encountered when solving the stationary Schrödinger equation in periodic potentials.

The significance of Floquet's theorem for solving the paraxial scattering equation is the following. It permits the computation of the fundamental matrix $\mathbf{\Psi}(z)$ and thus any wave function at any z provided that $\mathbf{\Psi}(z)$ is known in the interval $z\epsilon[0,a_z]$ by following the subsequent procedure. First, one has to compute a fundamental matrix of a sufficiently large number of linearly independent solutions within the first unit cell, e.g., by numerically integrating differently tilted plane waves through the first unit cell. Subsequently the fundamental matrix at any z may be obtained by virtue of (A3). The latter permits the computation of any solution to a given incoming wave because we can expand that wave into the particular set of linearly independent solutions forming the fundamental matrix. A numerical implementation of the above paraxial scattering algorithm has not been realized previously to our best knowledge.

APPENDIX B: SECOND-ORDER BORN APPROXIMATION

Here we provide an analytic argument for the observed shapes of the dynamically scattered wave's 3D Fourier spectrum, including in particular the existence of significant intensity around $\mathbf{k}=(0,0,na_z^{-1})$ with $n\epsilon\mathbb{N}$. We start with writing the Green's function G_0 and the propagator K_T of the free paraxial equation

$$\begin{aligned}G_0(\mathbf{r},z;\mathbf{r}',z')&=-i\Theta(z-z')K_T(\mathbf{r},z;\mathbf{r}',z')\\&=-\frac{\Theta(z-z')}{\lambda(z-z')}e^{i\frac{k}{2(z-z')}(\mathbf{r}-\mathbf{r}')^2}\end{aligned} \tag{B1}$$

as a solution to the inhomogeneous equation

$$\left(i\partial_z+\frac{1}{2k}\Delta\right)G_0(\mathbf{r},z;\mathbf{r}',z')=\delta(\mathbf{r}-\mathbf{r}')\delta(z-z'). \tag{B2}$$

We now expand the solution of the full paraxial equation into a Born series

$$|\Psi\rangle=|\Psi_0\rangle+\hat{G}_0\hat{U}|\Psi_0\rangle+[\hat{G}_0\hat{U}]^2|\Psi_0\rangle+\cdots.$$

Here the second term is the well-known first-order Born approximation and the third corresponds to the second-order Born approximation, accordingly. In the lateral 2D Fourier space the above symbolic expression reads

$$\begin{aligned}\Psi(\mathbf{k},z)\approx{}&2\pi\delta(\mathbf{k})+\frac{i}{v}\int\Theta(z-z')e^{i\frac{z-z'}{2k}\mathbf{k}^2}\Phi(\mathbf{k},z')dz'\\&-\frac{1}{v^2}\int\Theta(z-z')\Theta(z'-z'')e^{i\frac{z-z'}{2k}\mathbf{k}^2}\Phi(\mathbf{k},z')\\&\otimes_{\mathbf{k}}e^{i\frac{z'-z''}{2k}\mathbf{k}^2}\Phi(\mathbf{k},z'')dz'dz''.\end{aligned} \tag{B3}$$

Performing a Fourier transformation along z we finally obtain the following 3D Fourier space expression

$$\begin{aligned}\Psi(\mathbf{k})\approx{}&\sqrt{2\pi}^3\delta(\mathbf{k})\delta(k_z)\\&+\frac{i}{v}\left[\sqrt{\frac{\pi}{2}}\delta\left(k_z-\frac{\mathbf{k}^2}{2k}\right)+\frac{i}{\sqrt{2\pi}\left(k_z-\frac{\mathbf{k}^2}{2k}\right)}\right]\Phi(\mathbf{k},k_z)\\&-\frac{1}{v^2}\left[\sqrt{\frac{\pi}{2}}\delta\left(k_z-\frac{\mathbf{k}^2}{2k}\right)+\frac{i}{\sqrt{2\pi}\left(k_z-\frac{\mathbf{k}^2}{2k}\right)}\right]\Phi(\mathbf{k},k_z)\\&\otimes\left[\sqrt{\frac{\pi}{2}}\delta\left(k_z-\frac{\mathbf{k}^2}{2k}\right)+\frac{i}{\sqrt{2\pi}\left(k_z-\frac{\mathbf{k}^2}{2k}\right)}\right]\Phi(\mathbf{k},k_z).\end{aligned} \tag{B4}$$

The delta function $\delta(k_z-\frac{\mathbf{k}^2}{2k})$ occurring in the first-order Born approximation on the first line leads to the appearance of higher order Laue zones (HOLZ) lying on a parabolic (paraxial) Ewald "sphere." It is smeared out due to the second term occurring within the brackets of the first-order term. The second-order Born approximation explains the appearance of intensity at $\mathbf{k}=(0,0,na_z^{-1})$ at the center of the HOLZ. It originates from the convolution in reciprocal space producing a pronounced maximum in the middle of a HOLZ ring.

[1] H. A. Bethe, Ann. Phys. **392**, 55 (1928).
[2] E. Lamla, Ann. Phys. **424**, 178 (1938).
[3] J. Cowley and A. Moodie, Acta Cryst. **10**, 609 (1957).
[4] F. Fujimoto, J. Phys. Soc. Jpn. **14**, 1558 (1959).
[5] A. Howie and M. J. Whelan, Proc. R. Soc. London A **263**, 217 (1961).
[6] K. Fujiwara, J. Phys. Soc. Jpn. **16**, 2226 (1961).
[7] K. Kambe, Z. Naturforsch. **22a**, 422 (1967).
[8] M. V. Berry, J. Phys. C **4**, 697 (1971).
[9] D. Gratias and R. Portier, Acta Crystallogr., Sect. A **39**, 576 (1983).
[10] J. Cowley, *Diffraction Physics*, North-Holland Personal Library (Elsevier Science, Amsterdam, 1995).
[11] C. L. Jia, S. B. Mi, J. Barthel, D. W. Wang, R. E. Dunin-Borkowski, K. W. Urban, and A. Thust, Nat. Mater. **13**, 1044 (2014).
[12] J. Rusz, J.-C. Idrobo, and S. Bhowmick, Phys. Rev. Lett. **113**, 145501 (2014).
[13] J. Verbeeck, P. Schattschneider, and A. Rosenauer, Ultramicroscopy **109**, 350 (2009).
[14] K. W. Urban, J. Mayer, J. R. Jinschek, M. J. Neish, N. R. Lugg, and L. J. Allen, Phys. Rev. Lett. **110**, 185507 (2013).
[15] J. M. LeBeau, S. D. Findlay, L. J. Allen, and S. Stemmer, Phys. Rev. Lett. **100**, 206101 (2008).
[16] P. Stadelmann, Ultramicroscopy **21**, 131 (1987).
[17] C. Koch, Ph.D. thesis, Arizona State University, 2002.

[18] F. Houdellier, A. Altibelli, C. Roucau, and M.-J. Casanove, Ultramicroscopy **108**, 426 (2008).
[19] R. S. Pennington, F. Wang, and C. T. Koch, Ultramicroscopy **141**, 32 (2014).
[20] E. J. Kirkland, *Advanced Computing in Electron Microscopy* (Plenum Press, New York, 1998).
[21] J. H. Chen and D. Van Dyck, Ultramicroscopy **70**, 29 (1997).
[22] A. Rother and K. Scheerschmidt, Ultramicroscopy **109**, 154 (2009).
[23] C. Wacker and R. Schröder, Ultramicroscopy **151**, 211 (2015).
[24] P. Goodman and A. F. Moodie, Acta Crystallogr., Sect. A **30**, 280 (1974).
[25] D. V. Dyck, J. Microsc. **119**, 141 (1980).
[26] W. Greiner and J. Reinhardt, *Theoretische Physik, Vol. 7: Quantenelektrodynamik* (Verlag Harri Deutsch, Thun und Frankfurt am Main, 1984).
[27] M. O. De Beeck and D. Van Dyck, Phys. Status Solidi (a) **150**, 587 (1995).
[28] A. Rosenauer and M. Schowalter, *Microscopy of Semiconducting Materials 2007* (Springer, Netherlands, 2008), STEMSIM—a New Software Tool for Simulation of STEM HAADF Z-Contrast Imaging, p. 170.
[29] L. Allen, A. D'Alfonso, and S. Findlay, Ultramicroscopy **151**, 11 (2015).
[30] E. Kasper and P. W. Hawkes, *Principles of Electron Optics Vol. 3: Wave optics* (Academic Press, London, 1995).
[31] M. D. Graef, *Introduction to Conventional Transmission Electron Microscopy* (Cambridge University Press, Cambridge, 2003).
[32] W. Magnus, Commun. Pure Appl. Math. **7**, 649 (1954).
[33] G. Floquet, Annales de l'École Normale Supérieure **12**, 47 (1883).
[34] L. Peng, S. Dudarev, and J. Whelan, *High Energy Electron Diffraction and Microscopy*, Monographs on the Physics and Chemistry of Materials (Oxford University Press, Oxford, 2004).
[35] L. F. Shampine and M. K. Gordon, *Computer Solution of Ordinary Differential Equations: The Initial Value Problem* (W. H. Freeman, San Francisco, 1975).
[36] J. Rusz, S. Muto, and K. Tatsumi, Ultramicroscopy **125**, 81 (2013).
[37] X.-K. Wei, A. K. Tagantsev, A. Kvasov, K. Roleder, C.-L. Jia, and N. Setter, Nat. Commun. **5**, 3031 (2014).
[38] A. Weickenmeier and H. Kohl, Acta Cryst. **A47**, 590 (1991).
[39] I. Lobato and D. Van Dyck, Acta Crystallogr. Sect. A **70**, 636 (2014).
[40] A. Rother, T. Gemming, and H. Lichte, Ultramicroscopy **109**, 139 (2009).
[41] M. J. Whelan, J. Appl. Phys. **36**, 2103 (1965).
[42] C. Dwyer, Phys. Rev. B **89**, 054103 (2014).
[43] H. Kohl and H. Rose, Adv. Electron. Electron. Phys. **65**, 173 (1985).
[44] M. Nelhiebel, P.-H. Louf, P. Schattschneider, P. Blaha, K. Schwarz, and B. Jouffrey, Phys. Rev. B **59**, 12807 (1999).
[45] C. Dwyer, S. D. Findlay, and L. J. Allen, Phys. Rev. B **77**, 184107 (2008).
[46] J. Rusz, S. Bhowmick, M. Eriksson, and N. Karlsson, Phys. Rev. B **89**, 134428 (2014).
[47] We do not consider alternative integration schemes such as the Magnus expansion [32].
[48] Note that in the paraxial case considered here, the Ewald sphere is a paraboloid.